Scaling Hetero-Epitaxy from Layers to Three-Dimensional Crystals

Claudiu V. Falub, *et al.*

Science **335**, 1330 (2012);
DOI: 10.1126/science.1217666

Recently, room-temperature ionic liquids have been intensively studied as an attractive alternative to conventional electrolytes for ECs because of their high ion density, good thermal stability, and nonvolatility, as well as their wider potential window when compared with organic electrolytes (*14*, *32*). We fabricated an LSG-EC using the ionic liquid 1-ethyl-3-methylimidazolium tetrafluoroborate ($EMIMBF_4$) that exhibited a specific capacitance as high as 5.02 mF/cm^2 (276 F/$g_{LSG/electrode}$) and at a wider potential window of 4 V (fig. S16). A prototype LSG-EC was made and encapsulated in the $EMIMBF_4$ electrolyte, charged at a constant potential of 3.5 V, and used to light up a red LED for ~24 min (movie S1).

In order to demonstrate the overall performance of the LSG-ECs using various electrolytes, a Ragone plot is shown in Fig. 5 comparing the performance of LSG-ECs with different energy storage devices designed for high-power microelectronics. This includes a commercial 2.75 V/44 mF AC-EC and a 500-μAh thin-film lithium battery and a 3 V/300 μF aluminum electrolytic capacitor, all tested under the same dynamic conditions (SOM section 9). The plot shows the volumetric energy density and power density of the stack for all the devices tested. The LSG-EC can exhibit energy densities of up to 1.36 mWh/cm^3, a value that is approximately two times higher than that of the AC-EC. Additionally, LSG-ECs can deliver a power density of ~20 W/cm^3, which is 20 times higher than that of the AC-EC and three-orders of magnitude higher than that of the 500-μAh thin-film lithium battery. Although the electrolytic capacitor delivers ultrahigh power, it has an energy density that is three orders of magnitude lower than the LSG-EC. Because of the simplicity of the device architecture and the availability of the graphite oxide precursor, which is already manufactured on the ton scale, these LSG-ECs hold promise for commercial applications.

References and Notes

1. C. Liu, F. Li, L.-P. Ma, H.-M. Cheng, *Adv. Energy Mater.* **22**, E28 (2010).
2. D. S. Su, R. Schlögl, *ChemSusChem* **3**, 136 (2010).
3. P. Simon, Y. Gogotsi, *Nat. Mater.* **7**, 845 (2008).
4. J. R. Miller, P. Simon, *Science* **321**, 651 (2008).
5. D. Pech *et al.*, *Nat. Nanotechnol.* **5**, 651 (2010).
6. J. Chmiola, C. Largeot, P. L. Taberna, P. Simon, Y. Gogotsi, *Science* **328**, 480 (2010).
7. J. Xia, F. Chen, J. Li, N. Tao, *Nat. Nanotechnol.* **4**, 505 (2009).
8. M. Segal, *Nat. Nanotechnol.* **4**, 612 (2009).
9. M. D. Stoller, S. Park, Y. Zhu, J. An, R. S. Ruoff, *Nano Lett.* **8**, 3498 (2008).
10. Y. Wang *et al.*, *J. Phys. Chem. C* **113**, 13103 (2009).
11. Z. Weng *et al.*, *Adv. Energy Mater.* **1**, 917 (2011).
12. Y. Zhu *et al.*, *ACS Nano* **4**, 1227 (2010).
13. W. Gao *et al.*, *Nat. Nanotechnol.* **6**, 496 (2011).
14. C. G. Liu, Z. Yu, D. Neff, A. Zhamu, B. Z. Jang, *Nano Lett.* **10**, 4863 (2010).
15. Y. Zhu *et al.*, *Science* **332**, 1537 (2011).
16. X. Yang, J. Zhu, L. Qiu, D. Li, *Adv. Mater. (Deerfield Beach Fla.)* **23**, 2833 (2011).
17. V. Strong *et al.*, *ACS Nano* 120215095449007 (2012).
18. R. Chandrasekaran, Y. Soneda, J. Yamashita, M. Kodama, H. Hatori, *J. Solid State Electrochem.* **12**, 1349 (2008).
19. S. W. Lee, B. M. Gallant, H. R. Byon, P. T. Hammond, Y. Shao-Horn, *Energy Environ. Sci.* **4**, 1972 (2011).
20. H. Zhang, X. Yu, P. V. Braun, *Nat. Nanotechnol.* **6**, 277 (2011).
21. L. L. Zhang, X. S. Zhao, *Chem. Soc. Rev.* **38**, 2520 (2009).
22. P. L. Taberna, P. Simon, J. F. Fauvarque, *J. Electrochem. Soc.* **150**, A292 (2003).
23. Y. Shim, Y. J. Jung, H. J. Kim, *J. Phys. Chem. C* **115** 23574 (2011).
24. X. Zhao *et al.*, *J. Power Sources* **194**, 1208 (2009).
25. J. R. Miller, R. A. Outlaw, B. C. Holloway, *Science* **329**, 1637 (2010).
26. J. R. Miller, R. A. Outlaw, B. C. Holloway, *Electrochim. Acta* **56**, 10443 (2011).
27. C. Du, N. Pan, *J. Power Sources* **160**, 1487 (2006).
28. C. Du, N. Pan, *Nanotechnology* **17**, 5314 (2006).
29. H. Nishide, K. Oyaizu, *Science* **319**, 737 (2008).
30. D. W. Wang, F. Li, M. Liu, G. Q. Lu, H.-M. Cheng, *Angew. Chem. Int. Ed.* **47**, 373 (2008).
31. D. Andrea, *Battery Management Systems for Large Lithium Ion Battery Packs* (Artech House, Norwood, MA, 2010).
32. J. F. Wishart, *Energy Environ. Sci.* **2**, 956 (2009).

Acknowledgments: The authors thank the UCLA-based Focused Center Research Program in Functional Engineered NanoArchitectonics (R.B.K.) and the Ministry of Higher Education of Egypt (M.F.E.-K) for financial support, G. Gruner for valuable discussions, and B. Dunn, D. Membreno, and V. Augustyn for help with impedance and capacitance measurements.

Supporting Online Material

www.sciencemag.org/cgi/content/full/335/6074/1326/DC1
Materials and Methods
Figs. S1 to S16
References (*33*–*39*)
Movie S1

17 November 2011; accepted 9 February 2012
10.1126/science.1216744

Scaling Hetero-Epitaxy from Layers to Three-Dimensional Crystals

Claudiu V. Falub,[1]* Hans von Känel,[1] Fabio Isa,[2] Roberto Bergamaschini,[3] Anna Marzegalli,[3] Daniel Chrastina,[2] Giovanni Isella,[2] Elisabeth Müller,[4] Philippe Niedermann,[5] Leo Miglio[3]

Quantum structures made from epitaxial semiconductor layers have revolutionized our understanding of low-dimensional systems and are used for ultrafast transistors, semiconductor lasers, and detectors. Strain induced by different lattice parameters and thermal properties offers additional degrees of freedom for tailoring materials, but often at the expense of dislocation generation, wafer bowing, and cracks. We eliminated these drawbacks by fast, low-temperature epitaxial growth of Ge and SiGe crystals onto micrometer-scale tall pillars etched into Si(001) substrates. Faceted crystals were shown to be strain- and defect-free by x-ray diffraction, electron microscopy, and defect etching. They formed space-filling arrays up to tens of micrometers in height by a mechanism of self-limited lateral growth. The mechanism is explained by reduced surface diffusion and flux shielding by nearest-neighbor crystals.

Quantum structures based on epitaxially grown semiconductor layers are a playground for studying electron transport and optical properties, especially at low temperatures, where electron mobilities have reached values above 30 million cm^2/V•s (*1*). The discovery of fundamental phenomena such as the fractional quantum Hall effect (*2*) can be traced to the perfection of epitaxial heterostructures. Although progress has been faster for lattice-matched systems, the additional degree of freedom for band structure engineering offered by strain has become increasingly attractive. Nowadays, most state-of-the art microprocessors exploit strained Si (*3*).

The strain introduced by growing a single-crystalline layer of one material on a second crystal differing in lattice parameter can persist only up to a certain critical thickness (*4*, *5*). Beyond that thickness, segments of misfit dislocations form at the interface, gradually relieving the misfit strain as growth proceeds. Misfit dislocation segments are always accompanied by threading dislocations extending to the surface (*5*). From a practical point of view, threading dislocations are most undesirable, because they may penetrate active device regions far away from a dislocated interface. Numerous methods have been more or less successful in reducing threading dislocation densities (*6*–*18*).

Equally fundamental problems arise for applications requiring thick layers, such as high-brightness light-emitting diodes, power transistors, or multiple-junction solar cells. Different thermal expansion coefficients of layers and substrates then often cause layer cracking (*19*) and wafer bowing (*20*), prohibiting further wafer processing or causing device failure. Regarding these effects, frequently dwarfing the dislocation problem in practical importance, no satisfactory solution has been found to date.

In the quest for a viable path toward the monolithic integration of an x-ray imaging detector onto

[1]Laboratory for Solid State Physics, ETH Zürich, Schafmattstrasse 16, CH-8093 Zürich, Switzerland. [2]L-NESS, Department of Physics, Politecnico di Milano, via Anzani 42, I-22100 Como, Italy. [3]L-NESS, Department of Materials Science, Università di Milano-Bicocca, via Cozzi 53, I-20126 Milano, Italy. [4]Electron Microscopy Center, ETH Zürich, Schaffmattstrasse 16, CH-8093 Zürich, Switzerland. [5]Centre Suisse d'Electronique et Microtechnique, Jaquet-Droz 1, CH-2002 Neuchatel, Switzerland.

*To whom correspondence should be addressed. E-mail: cfalub@phys.ethz.ch

a complementary metal oxide semiconductor (CMOS) chip, we have developed a solution that may pave the way for the hetero-epitaxial growth of mismatched structures of any vertical scale onto any substrate. We consider the case of very thick Ge and SiGe layers deposited in a maskless process on a patterned Si(001) substrate. For pure Ge, the lattice and thermal expansion coefficient mismatches at room temperature are ~4.2% (*21*) and ~130% (*22*), respectively. We show that continuous films can be prevented from forming by growing far from equilibrium onto substrate features with high aspect ratios (i.e., height to base width). This results in a uniform space-filling array of three-dimensional (3D) epitaxial crystals, coalescence of which is avoided by self-limited lateral expansion, whereas their height, size, and shape can be tuned over a wide range by growth and substrate parameters. The observed piling up of crystalline material, dictated by kinetics and geometry, thus mimics 3D growth of bulk ingots on a micrometer scale.

Figure 1A shows an example of Ge crystals, grown on a periodic array of Si seeds. The seeds were formed by deep micromachining of (001)-oriented (within ±0.5°) Si substrates (*23*) into pillars from 1.7 to 8 μm in height, with base width from 0.75 to 15 μm and spacing from 200 nm to 50 μm. Scanning electron microscopy (SEM) images of 8-μm-tall and 2-μm-wide pillars are displayed in Fig. 1B. Subsequently, Ge was deposited epitaxially by low-energy plasma-enhanced chemical vapor deposition (LEPECVD) (*24*) at a high rate of 4 nm/s and growth temperatures T_G from 415° to 585°C (*23*). The SEM micrographs of Fig. 1C show arrays of Ge crystals grown on the two patterns of Fig. 1B. In contrast to the faceted crystals of Fig. 1A, they are shaped as flat-topped towers because of the lower growth temperature.

The deposition is highly nonconformal, characterized by self-limited lateral expansion near the bottom of the towers, subsequently evolving into vertical growth, irrespective of the amount of Ge material deposited and the details of the substrate patterns (Fig. 2A, and figs. S1 and S2) (*23*). The axes of the towers are defined by the growth direction, even when intentionally misoriented substrates (~6°) are used (fig. S3). The general shape of the towers is practically unaffected by the surface finishing (clean or oxidized) of the Si pillars, their sidewall roughness, and their exact orientation with respect to [001] (figs. S3 to S5). It does not even depend on the lattice and thermal mismatch, as a comparison of pure Si, $Si_{0.6}Ge_{0.4}$ alloy and pure Ge towers shows (fig. S6).

Depending on the choice of substrate pattern and the amount of material deposited, the arrays visible in Fig. 1C can cover almost the entire substrate surface, resulting in space fillings of up to 96%. By preventing the formation of a continuous layer, crack propagation and wafer bowing are inhibited, no matter how thick the epitaxial deposition. This can be seen in the Nomarski interference contrast image of Fig. 2B, showing the boundary between patterned and unpatterned regions of a 27-μm-thick layer. The continuous region (blue) exhibits many cracks due to the thermal stress developed during cool-down from the growth temperature, but no cracks have propagated into the patterned region (gray). The insets show expanded Nomarski and SEM views of Ge towers, exhibiting an aspect ratio of about 5.

In order to assess the crystal quality, tilt, and strain status of the Ge towers we used high-resolution x-ray diffraction, with reciprocal space mapping around the Si(004) and Si(224) reflections (*23*). The results provided evidence for the nearly perfect crystal structure of the towers and showed that the Ge material on the Si pillars is completely unstrained (figs. S7 to S9). The full relaxation of the thermal strain in the case of deposition on patterned Si substrates is likely to be purely elastic, provided by the high aspect ratio of the Ge towers, as confirmed by finite element method simulations (fig. S10) (*23*).

In order to understand which particular deposition features generate the growth and self-limited lateral expansion of Ge towers observed in Figs. 1 and 2 and figs. S1 to S7, we set up a 2D growth model based on a rate equation for the adatom phase, commonly used for interpreting facet growth in selective area deposition (SAD) experiments (*25*, *26*). In such an empirical model, the temporal variation of the adatom phase, which is usually a fraction of a monolayer, at a specific surface site is determined by the balance between the incoming flux, the incorporation rate into the crystal, the etching (or desorption) rate, and the diffusion from one site to another or from one facet to another (*23*).

The first key point in our experiments to be accounted for is the high deposition rate of 4 nm/s on (001) surfaces at low T_G (415° to 585°C). We estimate mean free paths for surface diffusion to be on the order of 100 to 200 nm in the time taken to deposit one monolayer, so that diffusion can be neglected on the scale of tower facets. Favored facets, typically {110}, {111}, {113}, and {001}, hence grow independently. The growth velocity perpendicular to a facet {*hkl*} is $v = \chi \cdot \Phi$, where χ is an incorporation factor, representing the net fraction of the incoming flux Φ incorporated into the solid under stationary conditions. This factor is related to the balance between crystallization and etching/desorption rates, which depend on the facet considered.

In addressing the flux Φ on different facets, we take into account both the velocity distribution of the activated gaseous species in the LEPECVD deposition chamber (*27*) and the inclination of each facet. Because of the large (compared to the pattern size) mean free path for the scattered molecules in the gas phase (some centimeters for average chamber pressures of $\sim 10^{-2}$ mbar), the total flux can be described as the superposition of a dominant isotropic part Φ_1, indicated by red arrows in Fig. 3A, and a uniform vertical contribution Φ_2, accounting for the preferential motion induced by charged species propagating from the plasma source to the sample (green arrows in Fig. 3A) (*27*). Their ratio is set to approximately 3:1, in order to account for the experimental accumulation at the bottom of the trenches (Fig. 3D), when progressive closure of the tower spacing is simulated. As a result, each facet experiences a different incoming flux Φ because of its orientation with respect to the vertical direction (fig. S11A).

The second key point of our experimental configuration is the additional reduction in the

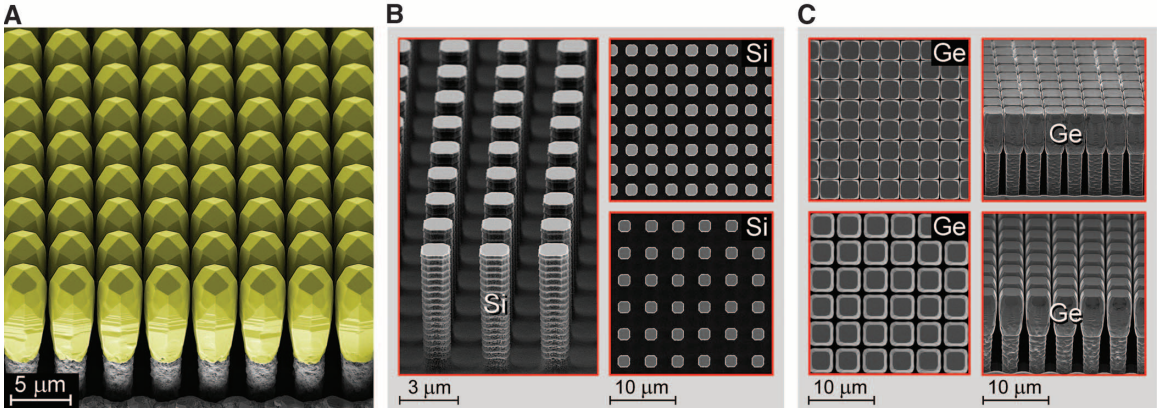

Fig. 1. Self-limited growth of Ge epitaxial crystals in the form of towers on deeply patterned Si(001) substrates. (**A**) Perspective-view SEM micrograph of 8-μm-tall Ge towers grown at 560°C on patterned Si wafers with 8-μm-tall and 2-μm-wide pillars, spaced by 2-μm trenches. (**B**) Perspective- and top-view SEM micrographs of 8-μm-tall pillars micromachined on Si(001) wafers by deep reactive ion etching. (**C**) Top- and perspective-view SEM micrographs of Ge towers grown at 415°C by LEPECVD on the Si pillars depicted in (B).

incoming flux by the shielding from neighboring towers, so that it is no longer uniform across a facet. After initial vertical and lateral growth, the flux component Φ_1 on vertical {110} facets is progressively reduced as the space between the Ge towers gets smaller (fig. S11B). This is accompanied by a progressive reduction of the lateral growth rate. As is well known from SAD literature (*28*), a facet extends in size when its growth velocity drops with respect to that of neighboring facets. To a lesser extent, the same happens to inclined {113} and {111} facets.

Figure 3B shows how the growth is simulated in a 2D model. We start from an initial distribution of {110}, {111}, {113}, and {001} facets, provided by SEM images at the early stages of the deposition. The resulting surface profile is partitioned into independent segments of ~150 nm. Perpendicular growth in the time step δt is $v \cdot \delta t$, where $v = \chi \cdot \Phi$ as defined above. Φ varies smoothly across a facet, mainly because of mutual tower shielding, but a larger variation occurs at the vertex between differently oriented facets (angle α and β for facet I and II, respectively, in Fig. 3B). Here, the segments are elongated up to their crossing point, in order to simulate the active intrasegment diffusion. If such a vertex (purple arrow in the bottom inset of Fig. 3B) stays within the green area as growth proceeds, both facets expand evenly, whereas one of them shrinks while the other expands if the vertex moves into a yellow area. This geometric condition, expressed by the angle θ in Fig. 3B, depends on the growth velocity ratio of the two adjacent segments. Therefore, the incorporation factors for inclined facets can be estimated by tracing the vertex evolution from the experimental SEM profiles for a single isolated pillar at different deposition stages (for example, the dashed white lines in Fig. 3C). In that case, Φ is determined by the facet inclination only, because flux shielding is absent. The incorporation factors for the inclined facets with respect to χ_{001} are found to be $\chi_{113} = 0.96$, $\chi_{111} = 0.89$, and $\chi_{110} = 0.78$ (*23*).

We used these fitted χ_{hkl} values to calculate the extended growth profiles in Fig. 3C (white lines superimposed on colored experimental SEM images) around an isolated pillar at different growth stages. The overall agreement is very good, especially for coverage below 10 μm.

By using the same χ_{hkl} values, and by taking into account the incoming flux shielding along the facets produced by nearby Ge towers, we simulated the shape evolution for a pattern with Si pillars spaced 4 μm apart. The excellent agreement between the experimental SEM profiles (in full color) and simulated (white lines) tower profiles (Fig. 3D and fig. S12) confirms the key role of geometric shielding. The vertical growth of the towers (see, for example, the SEM image in Fig. 2A) arises because the flux of activated gaseous species toward the {110} facets drastically drops when the spacing between towers shrinks below some tens of nanometers (fig. S1).

The surface filling of closely spaced but isolated towers is remarkably stable with respect to changes of the pattern geometry and variations in the deposition conditions. The surface morphology of the Ge towers can, however, be modified by careful tuning of the kinetic conditions. This becomes apparent from Fig. 4, A to C, showing SEM images of the substantial changes occurring with variations of T_G. Although the lowest T_G of 415°C (Fig. 4A) guarantees Ge towers with extended, flat (001) tops, progressive faceting sets in with increasing T_G, culminating in full {113} pyramidal tops at T_G = 585°C (Fig. 4C).

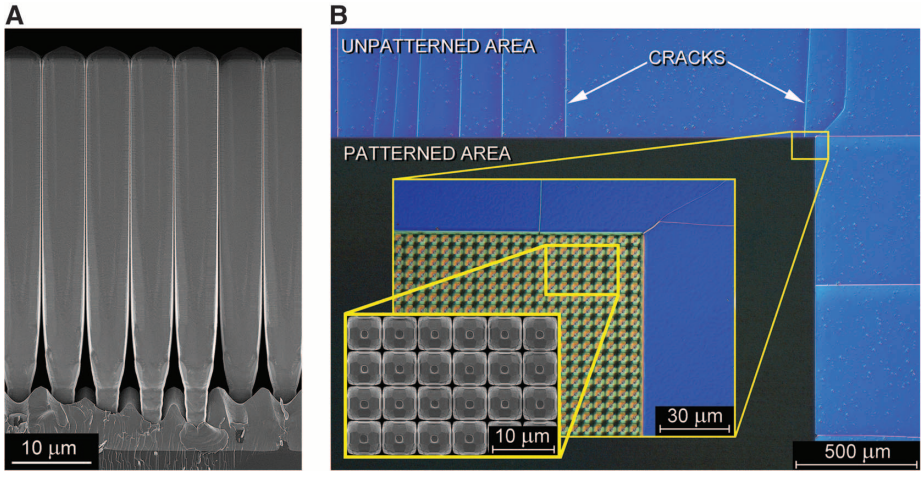

Fig. 2. Crack inhibition in a Ge/Si(001) system. (**A**) SEM micrograph of 50-μm-tall Ge towers, obtained by self-limited lateral growth at 490°C on a patterned Si substrate with 8-μm-tall and 2-μm-wide pillars, spaced by 4-μm trenches. (**B**) Nomarski interference contrast micrographs of 27-μm-tall Ge towers grown at 490°C on patterned Si substrates. Crack propagation stops at the border between patterned and unpatterned areas. The inset in the lower left corner is a top-view SEM micrograph of a few Ge towers.

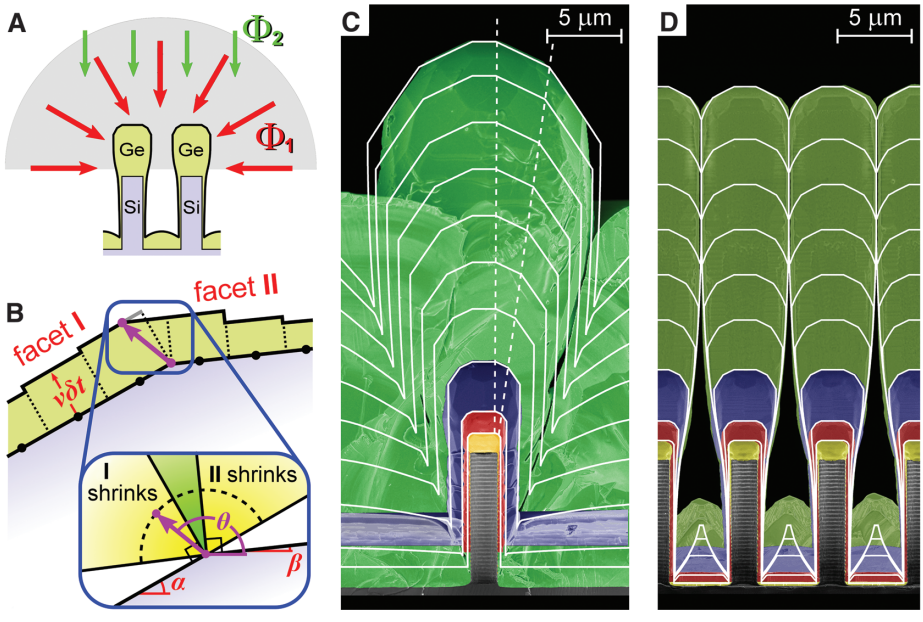

Fig. 3. Modeling of self-limited Ge tower growth. (**A**) Isotropic (red arrows) and vertical (green arrows) contributions to the incoming flux. Facet orientation and mutual shadowing among towers determine the effective flux at each surface region. (**B**) Sketch of a simulated profile at an edge between two neighboring facets, evolving in a time step δt. The facets are partitioned into segments, each one growing at its own velocity. Edges (purple arrow) evolve according to the ratio between facet growth velocities, as indicated in the inset, establishing a relation between geometric evolution and kinetic parameters. (**C**) The experimental facet evolution (colored SEM image) of an isolated Ge crystal grown at 490°C is used to fit the parameters of the model, yielding the profiles indicated by white lines at different growth stages. The edges between {001} and {113}, and {113} and {111} facets are indicated by dashed lines. (**D**) Simulated profile evolution (white lines) superimposed on experimental SEM images (full color) of Ge towers grown at 490°C on a patterned substrate with 2-μm-wide Si pillars, spaced by 4-μm trenches. In (C) and (D), the various colors correspond to different samples with different deposited thicknesses.

In the growth model outlined above, giving rise to simulated surface profiles in very good agreement with those seen experimentally (Fig. 3D), $v = \chi \cdot \Phi$ does not depend explicitly on temperature. The incorporation rate χ of each facet may, however, depend on T_G, as certainly does the surface diffusion between neighboring facets. A small amount of unbalanced surface flux can therefore result, provided that the facets differ favorably in terms of surface energy or adatom density. In order to estimate this effect, the ratio v_{113}/v_{001} of facet growth velocities was calculated from the temperature variation of the experimental profiles. The resulting ratios, displayed above the SEM images in Fig. 4, A to C, may be seen to vary only between 0.92 and 0.86 from the lowest to the highest T_G. This shows that slight variations of the relative velocities may cause drastic changes of the surface morphology.

Finally, we want to emphasize the key role of the tower morphology in controlling the threading dislocation density. The 60° dislocations present in crystals with the zincblende and diamond structures (*5*, *6*, *29*) have threading arms gliding in {111} planes and are directed along <110>. As indicated in the schematic drawing of Fig. 4D and in the cross-section transmission electron microscopy (TEM) images to its right, threading dislocations that are not parallel to [001] are geometrically expelled at the edges of 4-μm-wide and 8-μm-tall towers. Similar observations have been made in much smaller structures fabricated by SAD into dielectric windows on flat, unpatterned substrate surfaces exhibiting sufficiently large aspect ratios (*13*, *15*). This method is therefore also known by the name aspect ratio trapping (ART) (*15*). In contrast to experiments on ART, where the thickness of the dielectric and the submicrometer pattern size govern the attainable aspect ratio, this quantity may be tuned by varying the tower height in our case. In flat-top towers of the kind visible in the SEM images of Fig. 4A, additional dislocations may be present, oriented approximately along [001]. Examples of these so-called growth dislocations (*14*, *30*, *31*), remaining trapped along the entire tower height, may be seen in the TEM images in the lower right of Fig. 4D. Because cross-section TEM is poorly suited for an analysis of the threading dislocation density, we additionally used the method of etch pit counting. Indeed, an atomic force microscopy (AFM) analysis performed after defect etching revealed evenly distributed etch pits on the (001) top facets (upper right of Fig. 4D). Growth dislocations can only be expelled by surface faceting during growth (*14*), because they bend into directions perpendicular to a facet (see the schematic in Fig. 4E). This was shown to also be true for the submicrometer structures used in ART (*16*). We have demonstrated that the surface morphology of Ge towers can be controlled by adjusting T_G (Fig. 4, A to C). In the fully faceted towers obtained at higher T_G, the defects are indeed confined to the bottom part, according to the TEM images of Fig. 4E. The removal of threading dislocations from faceted Ge towers is confirmed by the absence of etch pits in AFM images such as that shown on the upper right of Fig. 4E.

The patterning of single-crystalline substrates into micrometer-sized features separated by deep trenches, combined with epitaxial deposition at a high rate, can lead to closely spaced crystals of arbitrary height by a mechanism of self-limiting lateral growth, thus mimicking the 3D growth of bulk ingots on a micrometer scale. We have shown for the Ge/Si(001) and SiGe/Si(001) systems that such a behavior is driven by geometric shielding of the incoming particle flux, combined with limited surface diffusion. Faceted Ge and SiGe crystals are dislocation-free and completely relaxed, despite the large lattice and thermal mismatch with the Si substrate. By avoiding the formation of continuous layers, wafer bowing and crack formation are inhibited. Although we have provided the proof of concept only for group IV semiconductors, we believe this new mode of hetero-epitaxial crystal growth to be applicable to most materials combinations used for the fabrication of semiconductor devices. We expect this to pave the way for many applications requiring thick hetero-epitaxial layers, such as x-ray and particle detectors monolithically integrated onto CMOS substrates, and power electronic devices or multijunction solar cells fabricated on cheap Si wafers.

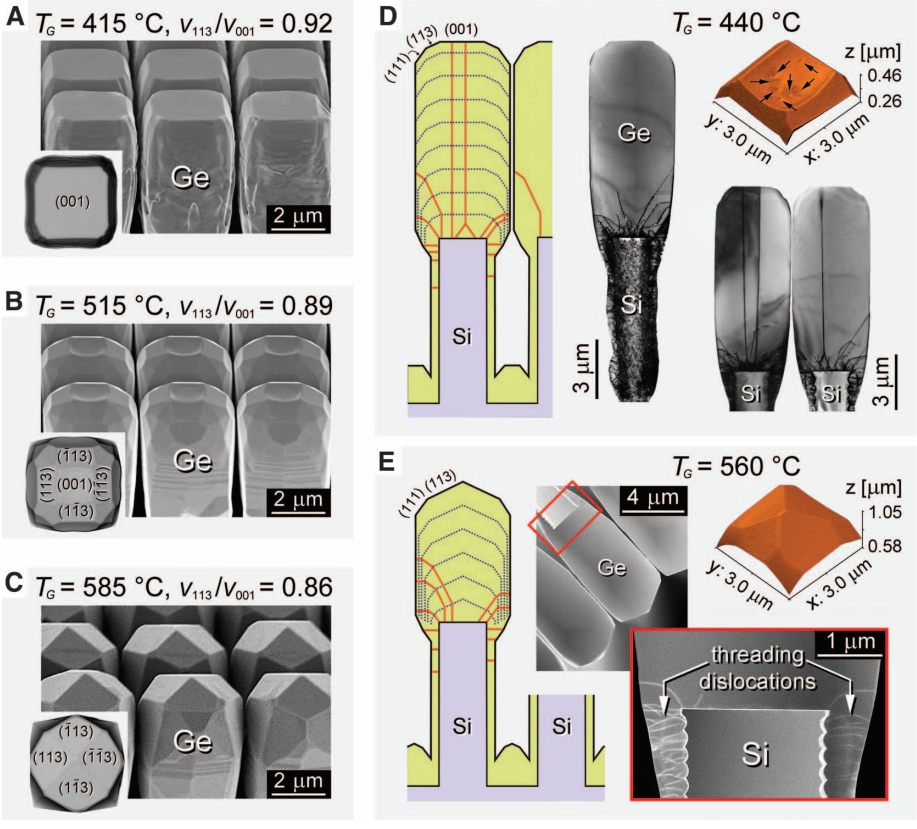

Fig. 4. Removal of threading dislocations by temperature-controlled faceting of the Ge towers. Shown are SEM micrographs of the surface morphology of Ge crystals evolving with increasing T_G, with flat tops at 415°C (**A**), partly faceted tops at 515°C (**B**), and full pyramidal shape at 585°C (**C**). The corresponding v_{113}/v_{001} velocity ratios derived from top-view and cross-sectional SEM micrographs vary from 0.92 to 0.86, as indicated. (**D**) (Left) Schematic drawing of growth dislocations trapped in Ge towers with (001) top facets, and of inclined dislocations escaping to the side walls. (Center) Brightfield TEM cross-section image acquired in the [2$\bar{2}$0] Bragg condition with inclined dislocations only. (Right) Corresponding TEM images with both kinds of dislocations, and an AFM micrograph taken after defect etching in an iodine solution. Etch pits are indicated by black arrows. (**E**) Schematic drawing (left), darkfield STEM images acquired along the [110] zone axis (middle), and AFM micrograph (right) for Ge crystals with only (113) and (111) facets. All dislocations are expelled from the crystals in this case, as confirmed by the absence of etch pits in the AFM image.

References and Notes

1. V. Umansky *et al.*, *J. Cryst. Growth* **311**, 1658 (2009).
2. H. L. Störmer, D. C. Tsui, *Science* **220**, 1241 (1983).
3. S. E. Thompson *et al.*, *IEEE El. Dev. Lett.* **25**, 191 (2004).
4. J. H. van der Merwe, *J. Appl. Phys.* **34**, 123 (1963).
5. J. W. Matthews, S. Mader, T. B. Light, *J. Appl. Phys.* **41**, 3800 (1970).
6. J. W. Matthews, A. E. Blakeslee, S. Mader, *Thin Solid Films* **33**, 253 (1976).
7. P. D. Hodson *et al.*, *Semicond. Sci. Technol.* **3**, 715 (1988).
8. E. A. Fitzgerald *et al.*, *Appl. Phys. Lett.* **59**, 811 (1991).
9. E. A. Fitzgerald, N. Chand, *J. Electron. Mater.* **20**, 839 (1991).
10. For a review of early work, see also (*31*).
11. M. R. Goulding, *Mater. Sci. Eng. B* **17**, 47 (1993).
12. H. C. Luan *et al.*, *Appl. Phys. Lett.* **75**, 2909 (1999).

13. T. A. Langdo *et al.*, *Appl. Phys. Lett.* **76**, 3700 (2000).
14. H. Klapper, *Mater. Chem. Phys.* **66**, 101 (2000).
15. J.-S. Park *et al.*, *Appl. Phys. Lett.* **90**, 052113 (2007).
16. J. Bai *et al.*, *Appl. Phys. Lett.* **90**, 101902 (2007).
17. S. Hu, P. W. Leu, A. F. Marshall, P. C. McIntyre, *Nat. Nanotechnol.* **4**, 649 (2009).
18. G. Wang *et al.*, *Appl. Phys. Lett.* **96**, 111903 (2010).
19. E. Feltin *et al.*, *Appl. Phys. Lett.* **79**, 3230 (2001).
20. M. Sakai, T. Egawa, M. Hao, H. Ishikawa, *Jpn. J. Appl. Phys.* **43**, 8019 (2004).
21. Y.-W. Mo, D. E. Savage, B. S. Swartzentruber, M. G. Lagally, *Phys. Rev. Lett.* **65**, 1020 (1990).
22. G. A. Slack, S. F. Bartram, *J. Appl. Phys.* **46**, 89 (1975).
23. Materials and methods and supporting text are available on *Science* Online.
24. C. Rosenblad *et al.*, *J. Vac. Sci. Technol. A* **16**, 2785 (1998).
25. M. Ohtsuka, S. Miyazawa, *J. Appl. Phys.* **64**, 3522 (1988).
26. S. Li, Q. Xiang, D. Wang, K. L. Wang, *J. Cryst. Growth* **157**, 185 (1995).
27. M. Rondanini *et al.*, *J. Appl. Phys.* **104**, 013304 (2008).
28. S. H. Jones, L. K. Seidel, K. M. Lau, M. Harold, *J. Cryst. Growth* **108**, 73 (1991).
29. E. P. Kvam, D. M. Maher, C. J. Humphreys, *J. Mater. Res.* **5**, 1900 (1990).
30. G. R. Booker *et al.*, *J. Cryst. Growth* **45**, 407 (1978).
31. A. Madhukar, *Thin Solid Films* **231**, 8 (1993).

Acknowledgments: Supported by the Swiss federal program funding Nano-Tera through project NEXRAY. Partial support from Fondazione CARIPLO within the MANDIS Project is gratefully acknowledged. We thank Centre Suisse d'Electronique et Microtechnique, Neuchatel, for providing most of the patterned Si substrates used in this work; D. Colombo for preparing the patterned substrates with the submicrometer-wide Si pillars and trenches by means of cryogenic deep reactive ion etching; M. Meduňa for his help in performing and analyzing the synchrotron submicrometer diffraction experiments; B. Batlogg, A. Dommann, A. Neels, R. Kaufmann, A. Pézous, F. Montalenti, F. Pezzoli, E. Bonera, R. Gatti, A. G. Taboada, and T. Kreiliger for valuable discussions; A. Fedorov and K. Mattenberger for technical support; the FIRST Center for Micro- and Nanoscience of ETH Zürich for making available its infrastructure; and the scientific personnel at the ID01 beamline of the European Synchrotron Radiation Facility, Grenoble, in providing user support for the submicrometer diffraction experiments. International patent application WO 2011/135432 has been filed.

Supporting Online Material
www.sciencemag.org/cgi/content/full/335/6074/1330/DC1
Materials and Methods
SOM Text
Figs. S1 to S12
References (*32*–*36*)

8 December 2011; accepted 27 January 2012
10.1126/science.1217666

A Change in the Geodynamics of Continental Growth 3 Billion Years Ago

Bruno Dhuime,[1,2]* Chris J. Hawkesworth,[1] Peter A. Cawood,[1] Craig D. Storey[3]

Models for the growth of continental crust rely on knowing the balance between the generation of new crust and the reworking of old crust throughout Earth's history. The oxygen isotopic composition of zircons, for which uranium-lead and hafnium isotopic data provide age constraints, is a key archive of crustal reworking. We identified systematic variations in hafnium and oxygen isotopes in zircons of different ages that reveal the relative proportions of reworked crust and of new crust through time. Growth of continental crust appears to have been a continuous process, albeit at variable rates. A marked decrease in the rate of crustal growth at ~3 billion years ago may be linked to the onset of subduction-driven plate tectonics.

The timing, rates, and the geodynamical conditions of continental crust generation, destruction, and reworking remain a topic of considerable debate (*1*–*7*). The variations in radiogenic isotope ratios in detrital rocks and minerals are a key archive of the continental record (*3*–*5*, *8*), and the rapid increase in the numbers of U-Pb and Hf isotope analyses of predominantly detrital zircons have provided new constraints for models of crustal evolution (*4*). Hf isotopes in U-Pb–dated zircons are commonly used to characterize the nature of the source of the magma from which the zircon crystallized and to determine the time since this source separated from the upper mantle, commonly referred to as the model age of crust formation (*9*–*11*). However, individual model ages may not represent true periods of crust formation (*12*) because the crustal material analyzed may represent mixtures of older "reworked" and new juvenile material. Continental growth models based simply on U-Pb and Hf isotopes in zircon therefore have a large uncertainty over the proportions of new continental crust generated in different magmatic episodes, and hence over the shape of the continental growth curve (*4*).

Combining stable isotopes, such as oxygen, with the radiogenic isotopes of U-Pb and Lu-Hf (*6*, *13*) may reduce uncertainties surrounding the proportion of new and reworked crust. "Mantle-like" zircons, that is, zircons that crystallized from mantle-derived magmas, have a narrow range of $^{18}O/^{16}O$ (expressed as $\delta^{18}O$ relative to Vienna standard mean ocean water), typically $\delta^{18}O = 5.3 \pm 0.6‰$ (per mil) (2 SD) (*14*). When their parent magmas contain a contribution of sedimentary material or source rocks altered by low- (or high-) temperature hydrothermal activity, the $\delta^{18}O$ in zircons can range to higher (or lower) values (*15*). In principle, periods of juvenile crust formation should be characterized by zircons with mantle-like $\delta^{18}O$ and similar radiogenic Hf model ages (*6*). Conversely, periods dominated by crustal reworking result in the generation of "supracrustal" zircons, typically with elevated $\delta^{18}O$ values and varying Hf model ages (*13*, *15*, *16*). To the extent that Hf isotope ratios of supracrustal zircons represent mixtures, they will not record true periods of crustal growth (*6*). There are relatively few studies in which U-Pb and Hf isotopes are combined with O isotopes in zircon (*6*, *7*, *17*, *18*), and evaluating crustal growth models based on large data sets of zircons remains difficult, especially when constraining the proportions of new crust formation ages to those that are arguably hybrid ages (*4*, *8*, *19*).

$\delta^{18}O$ values are plotted as a function of Hf model ages in 1376 detrital and inherited zircons from Australia, Eurasia, North America, and South America (Fig. 1A) (*11*). These data are taken to be representative of the Hf-O isotope record available for Earth's continental crust. Overall supracrustal zircons with Meso/Paleo-Proterozoic Hf model ages show a greater range of $\delta^{18}O$ values than those with older or younger model ages, and they are more abundant than mantle-like zircons. The proportions of mantle-like zircons and supracrustal zircons in turn determines the relative proportions of new crust formation ages and hybrid model ages induced by crustal reworking processes in the distribution of Hf model ages (Fig. 1B). The proportion of new crust formation ages does not change substantially in the first billion years of Earth's history, with a median value ~73%. From ~3.2 billion years ago (Ga), the proportion of new crust formation ages gradually decreases down to ~20% at ~2 Ga, and it then increases to ~100% toward the present day (Fig. 1B). Assuming that these observations characterize the continental crust as a whole, this parameterization allows us to predict the proportion of new crust and hybrid model ages throughout Earth's evolution and, hence, access the large U-Pb and Hf isotope data sets that do not include $\delta^{18}O$ data (*4*, *8*, *19*).

Young sediments typically contain zircons with a wide range of ages, so they appear to provide records that are more representative of the magmatic history of the crust than zircons in igneous rocks or in old sediments (*5*). A compilation of 6972 analyses of detrital zircons with deposition ages ranging from the late Paleozoic to the present day (*11*) results in a distribution of Hf model ages that does not simply reflect the generation of new crust, because it still includes

[1]Department of Earth Sciences, University of St. Andrews, North Street, St. Andrews KY16 9AL, UK. [2]Department of Earth Sciences, University of Bristol, Wills Memorial Building, Queens Road, Bristol BS8 1RJ, UK. [3]School of Earth and Environmental Sciences, University of Portsmouth, Burnaby Road, Portsmouth PO1 3QL, UK.

*To whom correspondence should be addressed. E-mail: b.dhuime@bristol.ac.uk